Available online at www.sciencedirect.com

SCIENCE DIRECT®

Journal of Magnetic Resonance 171 (2004) 25–36

JMR Journal of Magnetic Resonance

www.elsevier.com/locate/jmr

A phase cycle scheme that significantly suppresses offset-dependent artifacts in the R_2-CPMG ^{15}N relaxation experiment

Grover N.B. Yip[a], Erik R.P. Zuiderweg[a,b,c,*]

[a] Department of Chemistry, University of Michigan—Biophysics Research Division 930 N. University Ave, Ann Arbor, MI 48109, USA
[b] Department of Biophysics, University of Michigan—Biophysics Research Division 930 N. University Ave, Ann Arbor, MI 48109, USA
[c] Department of Biological Chemistry, University of Michigan—Biophysics Research Division 930 N. University Ave, Ann Arbor, MI 48109, USA

Received 15 April 2004; revised 19 May 2004
Available online 24 August 2004

Abstract

R_2-CPMG ^{15}N relaxation experiments form the basis of NMR dynamics measurements, both for analysis of nano–pico second dynamics and milli–micro second dynamics (kinetics). It has been known for some time that in the practical limit of finite pulse widths, which becomes acute when using cryogenic probes, systematic errors in the apparent R_2 relaxation behavior occur for spins far off-resonance from the RF carrier. Inaccurate measurement of R_2 rates propagates into quantitative models such as model-free relaxation analysis, rotational diffusion tensor analysis, and relaxation dispersion. The root of the problem stems from evolution of the magnetization vectors out of the XY-plane, both during the pulses as well as between the pulses. These deviations vary as a function of pulse length, number of applied CPMG pulses, and CPMG inter-pulse delay. Herein, we analyze these effects in detail with experimentation, numerical simulations, and analytical equations. Our work suggests a surprisingly simple change in the phase progression of the CPMG pulses, which leads to a remarkable improvement in performance. First, the applicability range of the CPMG experiment is increased by a factor of two in spectral width; second, the dynamical/kinetic processes that can be assessed are significantly extended towards the slower time scale; finally, the robustness of the relaxation dispersion experiments is greatly improved.

Keywords: CPMG; Offset dependent artifacts; Transverse (T_2) relaxation; Phase cycle; Relative accuracy; Bloch simulations; Relaxation dispersion

1. Introduction

The characterization of protein dynamics helps to correlate structural properties with biological activities [1–3]. For instance, enzyme active sites often contain protein loops, which are by nature dynamic [4–10]. Allosteric proteins by definition take part of their function from dynamical changes [11]. NMR has developed into a tool in which these dynamical processes can be measured on an atom-resolution scale, leading to order parameters, time scales, motional models, models for correlated motion, and estimations of conformational entropy. NMR CPMG R_2-relaxation experiments are key to virtually all of these dynamical investigations. It is an indispensable experiment in the investigations of picosecond dynamics using model-free spectral density estimation [12–14] or SLRS data analysis [15,16]; and it is one of the only two possible experiments to measure R_2-relaxation dispersion [17–20] giving insight into microsecond–millisecond dynamics. In the former case, ideally, the CPMG cycle completely suppresses chemical (conformational) exchange processes; in the latter, ideally, the CPMG pulse sequence should provide identical

---

[*] Corresponding author. Fax: +1 734 764 3323.
E-mail address: zuiderwe@umich.edu (E.R.P. Zuiderweg).

1090-7807/$ - see front matter © 2004 Elsevier Inc. All rights reserved.
doi:10.1016/j.jmr.2004.06.021

spin-physics effects over the entire sample, independent of NMR resonance offset, and inter-pulse delay.

However, to preserve the probe and sample during the CPMG cycle, one is typically restricted to a maximum of 3000 Hz B_1 field for the ^{15}N pulses (83 μs 90° pulse), leading to an effective field tilted away from the pulse axis by 14° or 22°, with flip angles of 186° or 194° at the edge of the ±15 ppm ^{15}N spectral range on a 500 or 800 MHz instrument, respectively. The recommended limits on ^{15}N power deposition in cryogenic probes calls for even longer pulse lengths (100 μs 90° pulses, see below). Consequently, the spin physics is strongly dependent on the offset. Yet, in practice, it is generally assumed that these systematic offset errors influence the peak intensities in the NMR spectrum equally for all time points in the relaxation curve (i.e., as the number of CPMG pulses is varied), and hence do not affect the relaxation rates. That this assumption is unjustified is demonstrated as follows.

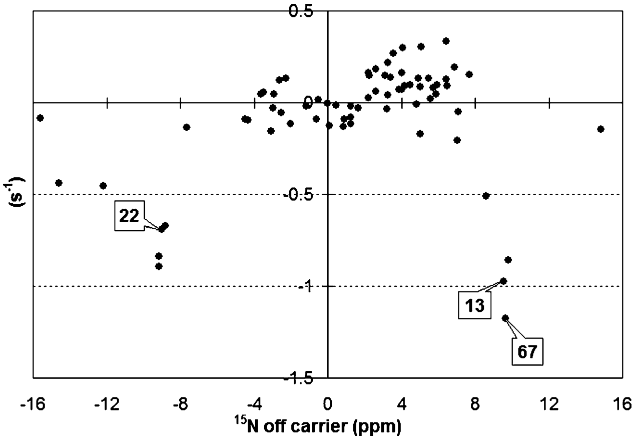

Fig. 2. The difference of the conventional R_2 CPMG experiment, and the multiple on-resonance R_2 CPMG experiment (Fig. 1) plotted as a function of ^{15}N ppm offset from the carrier. Labeled points indicate the residue numbers highlighted in Fig. 1.

In Fig. 1, we compare the R_2-CPMG rates for the ^{15}N resonance of ubiquitin measured in the conventional way with the ^{15}N carrier in the center of the ^{15}N spectrum (117.8 ppm) with the results of 29 separate R_2-CPMG experiments in which we placed the ^{15}N carrier at 29 different positions in the ^{15}N spectrum, approaching an "on-resonance R_2-CPMG" for each individual residue of the protein. The figure shows that large differences exist between the R_2 rates obtained in these two ways for about 20 residues. When the differences in rates between the two experiments are plotted vs. the ^{15}N resonance offset in Fig. 2, it becomes evident that the deviations correlate with the RF offset. The basis of the problem is that the number of CPMG pulses employed increases as a function of the relaxation decay delay, causing a systematic increase of the RF pulse offset artifacts, hence affecting the accuracy of the decay curves for spins resonating further from the carrier. The artifacts are of a magnitude that can easily lead to the wrong conclusions with respect to protein dynamics on both the nanosecond timescale as well as on the millisecond time scale: what appears as a local dynamical effect for a particular residue in a protein may in reality be due to the RF offset of the ^{15}N resonance of the residue in question. Moreover, the artifacts will certainly interfere with the very small variations in R_2/R_1 ratios that may be exploited to determine the rotational diffusion tensor of the biomolecule. We are not the first to report these

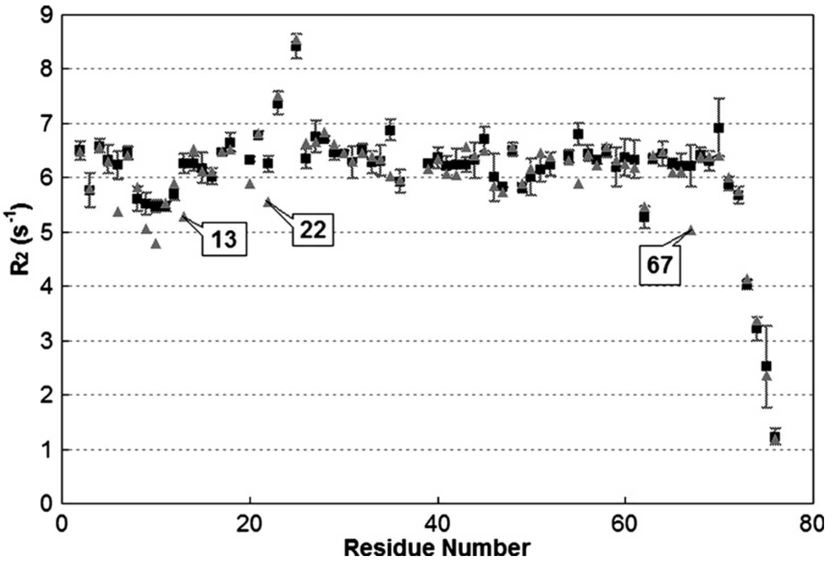

Fig. 1. R_2 residue profile plot for ubiquitin. Light triangles depict a conventional experiment, i.e., the profile obtained from a single R_2 experiment. Dark squares were obtained via the 'multiple on-resonance CPMG experiment' procedure. Parameters used: ^{15}N 180° pulse: 200 μs; τ_{cp}, 700 μs. (See Fig. 3). Labeled points indicate the residue numbers highlighted in Fig. 2.

artifacts [21–23], but our contribution differs from the previous ones that we analyze the causes of the artifacts in detail (we distinguish two separate causes) and suggest an experimental solution to the problem. The major artifacts are caused by intermixing of R_1 relaxation with R_2 relaxation because spins that are off-resonance will have their magnetization vectors perturbed out of the transverse plane. This situation is not unlike the $T_{1\rho}$ experiments, where R_1 also becomes mixed with R_2 as a function of resonance offset. Unlike the $T_{1\rho}$, however, no simple analytical relationship can be derived to correct for the systematic errors in the R_2 CPMG offset dependence. Herein, we are *not* suggesting the trivial solution to use multiple carrier offsets such as in Fig. 1, because of obvious practical drawbacks, although varying the carrier to obtain data at extreme offsets maybe still be useful. Neither are we suggesting the other trivial solution to use very strong RF pulses, as that is likely detrimental to the equipment and sample. Instead, we show by experiment and numerical simulation that a simple change in phase cycling scheme can suppress all artifacts simultaneously, and improve the applicability range of the R_2-CPMG experiment by a factor of two in spectral width for the same carrier and power settings.

2. Materials and methods

2.1. Spectroscopy

All experiments were obtained using ^{15}N-labeled human ubiquitin (20 mg/ml in a 90% H_2O/10% D_2O solution, pH 5.2, Martek), on a Bruker Avance 500 MHz spectrometer at a sample temperature of 298 K. All experiments were carried out using a duty-cycle compensated ^{15}N R_2 CPMG experiment (Fig. 3), analyzed in detail in a forthcoming manuscript.

Conventional R_2 CPMG sets were obtained with the ^{15}N carrier placed at 117.846 ppm. Each relaxation decay set (RDS) was obtained with three decay points for total decay times of 5.6, 33.6, and 98 ms periods (including pulse lengths) or 2, 12, and 35 CPMG-period loops, respectively. Finally, the time-dependent intensities of corresponding peaks (residue signal) are fitted to single exponentials to obtain the experimental rates.

For the "multiple on-resonance CPMG experiment" (Fig. 1), 29 RDSs were collected with the ^{15}N carrier frequency offset incremented every 50 Hz (~1 ppm) starting at 5272.8734 Hz (~104.3 ppm). This process yielded 29 '^{15}N strips' of 1 ppm wide 'on-resonance' spectra, collectively covering a spectral width of 29 ^{15}N ppm unit frequency range centered about 117.846 ppm. This will suffice to provide reasonably ideal measurements for the complete human ubiquitin spectrum. By this method, one can construct an ideal R_2 rate vs. residue plot. An otherwise identical series of 29 RDS was carried out using a different phase cycling for the CPMG pulses (see details in Fig. 1).

^{15}N resonances that lie within ±2 ppm (~ ± 13° off-resonance) of the carrier frequency are collected from all 29 RDSs and used to represent the collection of "true" on-resonance relaxation values; peaks appearing within two or more ±2 ppm strips were averaged. Reference measurements for each distinct and unambiguously assigned peak were obtained for the following categories; 5.6 ms decay peak intensities, 33.6 ms decay peak intensities, 98 ms decay peak intensities, and R_2 rate values.

2.2. Numerical simulations

Simulations of the nuclear spin vector behavior in a magnetic field, during the R_2 relaxation mixing time loop only, was computed via numerical integration of the rotating-frame Bloch equations Eqs. (1)–(4) [24]:

$$\frac{dM_x}{dt} = \left(\pm\omega^{\mathrm{rf}}_{\pm y} M_z - \omega_{\mathrm{FP}} M_y\right) + R_2(M_x), \qquad (1)$$

$$\frac{dM_y}{dt} = \left(\mp\omega^{\mathrm{rf}}_{\pm x} M_z + \omega_{\mathrm{FP}} M_x\right) - R_2\left(M_y\right), \qquad (2)$$

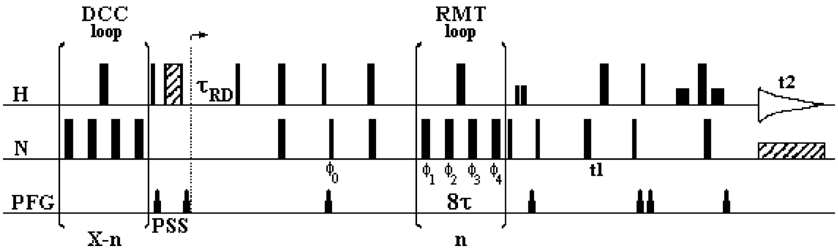

Fig. 3. R_2-CPMG experiment, as described in detail in a forthcoming manuscript, serving to maintain constant sample temperature by keeping the total number of pulses constant for any relaxation delay. RMT, relaxation mixing time; DCC, duty cycle compensation; and PSS, pre-scan saturation. Either of the following two phase schemes were utilized: (1) Traditional, 0000, $\phi_0 = \pm X$ and $\phi_1 = \phi_2 = \phi_3 = \phi_4 = +X$ or (2) 0013, $\phi_0 = \pm X$ and $[\phi_1, \phi_2, \phi_3, \phi_4] = [+X, +X, +Y, -Y]$. All experiments were ran with a recovery delay (τ_{RD}) of 0.75 s, at 8 transients per t_1, with acquisition decoupling enabled and a constant overall duty cycle density ensured by DCC + RMT = constant = 36 loops. All experiments were acquired for the duration of 245.8 ms with (128 × 4096) total complex points and spectral widths of (3333.33 × 8333.33) Hz in the ($t_1 \times t_2$) dimensions, respectively, for a general run time of 41–42 min per 2-D spectrum. The T_2-CPMG (RMT) loops ran with repeat time of $\tau = \tau_{\mathrm{cp}}/2 = 350$ μs, and a 200 μs ^{15}N π pulse.

$$\frac{\mathrm{d}M_z}{\mathrm{d}t} = \left(\pm\omega^{\mathrm{rf}}_{\pm x} M_y\right) - R_1(M_z - M_0) \tag{3}$$

or

$$\frac{\mathrm{d}M_z}{\mathrm{d}t} = \left(\mp\omega^{\mathrm{rf}}_{\pm y} M_x\right) - R_1(M_z - M_0), \tag{4}$$

in which ω_{FP} is the free precession offset; and R_1 and R_2 are the longitudinal and transverse rate constants, respectively. $\omega^{\mathrm{rf}}_{\rho}$ is the radio frequency (RF) pulse amplitude, with the ρ phase depending upon the CPMG pulse phase desired ($\rho = +X(0), +Y(1), -X(2)$, or $-Y(3)$). Eqs. (3) or (4) was used depending on the applied RF phase. The initial magnetization was assumed to lie perfectly along either the + or $-X$-axis for all simulations.

The numerical integrations of the set of coupled differential Bloch equations were calculated using in-house developed Fortran 77 code. Simulations were performed to compare theoretical to experimental observations as well as provide a flexible means to test experimental innovations. Additionally, detailed simulations were sustained to expand on the understanding of spin dynamics and how the spin behaves throughout the relaxation period by monitoring the behavior of the spin vector trajectory evolution over time.

The simulation code focuses on a single spin echo, which is looping onto itself to simulate the desired number of spin echoes. It is assumed that the potential problems in any part of the pulse scheme before and after the relaxation loop period (see Fig. 3) are negligible or constant. It was established that it was not necessary to take the scalar coupling between ^{15}N and ^{1}H into account; good correspondence with the experimental data was obtained without it. Furthermore, it was assumed that ^{15}N–^{1}H cross-correlated cross-relaxation is sufficiently suppressed by the 180° proton pulses in the actual experiment, and was consequently not considered in the simulation.

Various techniques were used in order to realistically mimic the actual experiments. First it is required to calculate the average of $+X$ and $-X$ initial ^{15}N magnetization simulated R_2 values, in order to emulate the phase cycling of the first ^{15}N 90° pulse in the actual experiment. Second, in lieu of the possibility that spin systems at destined offset frequency from the carrier can experience irregular relaxation decay profiles (Fig. 4), only the decay points of total decay times that correspond to experimental decay points are ultimately used in the calculation of the R_2 rate fits. Furthermore, averaging the R_2 rates of discrete points covering the range of the effective flip angle were used to simulate RF inhomogeneity in the sample tube.

Ultimately, to simulate the systematic R_2 RF offset dependency profile, a series of R_2 rates was calculated for a range of incremented offset frequency settings. In short, the signal intensities as a function of offset were calculated with an increasing number of CPMG pulses, and the time-dependent intensities at each offset point fitted with single exponentials to obtain the theoretical offset-dependent rates. For thorough coverage of a typical ^{15}N ppm protein spectral width, R_2's were calculated every 0.313 ppm or effectively incremented every 2° offset from the carrier, ranging from −30 to 30 ppm off-resonance. The experimental global averages of R_2 and R_1 rates for ubiquitin, determined from previous observations, were used in the Bloch equation simulations, both in the presence and absence of the RF pulses. In the final analysis there was an R_2 of approximately 6 s^{-1} and an R_1 of 2.4 s^{-1}. The 200 μs ^{15}N 180° pulses, unattainable 25 μs ^{15}N 180° pulses and infinite power instantaneous pulse (0 μs), offset dependence profiles have been explored thoroughly. The 200 μs ^{15}N 180° pulses were chosen as a practical value, because our simulations are made anticipating CPMG experiments with maximum exchange suppression, i.e., short τ_{cp}, using a cryogenic probe. The values chosen are rationalized as follows: our manufacturer (Bruker) recommends for their cryoprobes windowless ^{15}N pulse trains at a maximum power level corresponding to a 200 μs 90° pulse. The 200 μs ^{15}N 180° pulses require a 4-fold increase in RF power relative to this maximum, thus calling for a duty cycle of 25%, which allows the desired short, 600 μs, τ_{cp} intervals. Our calculations below for maximum suppression rates are slightly more conservative than these settings, i.e., 200 μs 180° pulses with 700 μs (τ_{cp}) intervals. The effect of longer τ_{cp} settings with the same pulse length was also investigated, as it models relaxation dispersion experiments using cryogenic probes [18,20].

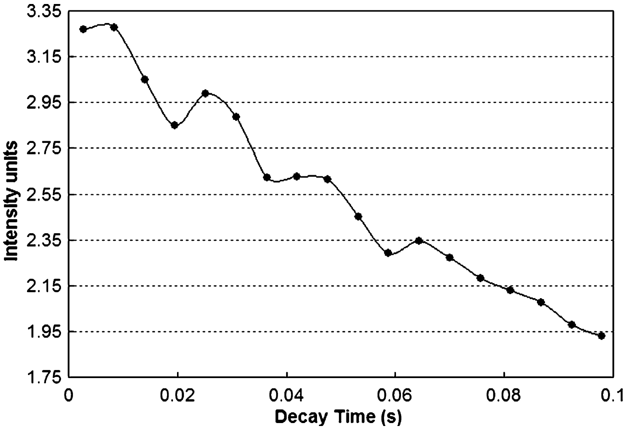

Fig. 4. The experimental decay profile for residue Ala46 at +14.842 ppm (~94.78° at the center of the pulse or 67.7° after τ_{FP}) offset from the ^{15}N carrier (117.846 ppm) from a single RDS of 18 decay points (2.8–98 ms in increments of 5.6 ms) using the traditional all $+X$-phase.

Last but not least, instantaneous, hard, and soft RF pulse perturbation strengths were calculated in combination with the four RF pulse phases, 0, 1, 2, and 3 to observe all echo evolution types (i.e., anti-parallel/parallel or $+Z/-Z$ orthogonal evolution).

2.3. Data analysis

A systematic R_2 dependence profile as a function of offset from the carrier may be observed from a single residue from each of the 29 RDSs of the same phase cycle, but this is an extremely scarce representation of the dependence profile (not shown). Fortunately, there are actually greater than 2000 R_2 values measured as a function of offset (70 unambiguous peaks per RDS), all of which can be collected and averaged so that the 2030 observations can be used to exemplify overall experimental R_2 dependence profile as a function of resonance offset. This is achieved by applying standardization techniques described below.

It is reasonable to assume that there exists a true R_2 rate profile and that it can roughly be represented by the reference R_2 values described above. By standardizing (shifting) the reference R_2 magnitude of each peak in the profile to a standardized value and applying the same shift to each of the corresponding residue measurements from all the RDS profiles, the result is a peak standardized quantity or essentially a suppression of the peak R_2 magnitude variability within each RDS. Moreover, the adjusted quantity still retains the original carrier offset setting and systematic dependence characteristics such that each measurement in the peak profile for all RDSs can be exploited in the same dependence profile series, thus, a more detailed off-resonance R_2 profile can be observed experimentally. One can appreciate the invaluable practice of this type of analysis because a single spectrum can give rise to a large 'sample' of offset measurements covering a respectable offset range (Fig. 2).

Additionally, there are two types of measurements to distinguish, each requiring distinctly different standardization procedures. First, is the shifting procedure (Procedure 1) just described above which applies to observations that are uniquely independent and expectedly constant quantities (e.g., relaxation rates and reproducibility measurements) and can be standardized by 'virtual shifting' of the observable magnitudes. Second, is the scaling procedure (Procedure 2)—essentially replacing +/− with ×/÷, respectively, in (Procedure 1)—which applies to standardization of individual observable quantities that are also distinctly dependent on a secondary relationship (e.g., a set of distinct peak intensity magnitudes with varying relaxation decay characteristics from a single decay point spectrum) and must be scaled by a ratio factor. Specifically, the intensity of each peak, within a spectrum of one decay point in a RDS, is distinctly different in two ways; first is the intrinsic $\frac{1}{2}$ spin population difference or the signal magnitude, and second is the spin decay characteristic or the extent of the expected decay loss that is dependent upon the decay point/RMT period. To standardize this type of observable both the signal magnitude and the decay characteristic needs to be standardized, and the scaling procedure accomplishes that:

$$((\text{Standardized goal}) - (\text{Reference value})) + (\text{Raw value}) \qquad (\text{Procedure1})$$

$$((\text{Standardized goal}) \div (\text{Reference value})) \times (\text{Raw value}) \qquad (\text{Procedure2})$$

3. Results and discussion

Simulations of the R_2-CPMG decays (Fig. 5), using numerical integration of the Bloch equations for similar parameters as the experiment in Fig. 1 and described in Section 2, do reproduce the experimental offset dependence of the apparent R_2 quite well. To examine the sources of error we make the first simplification in Fig. 6 by neglecting sample inhomogeneity.

Fig. 6 clearly reveals two different fluctuations as a function of offset. First, there is a slow oscillation with a "frequency" of 7 ppm that is caused by admixture of R_1 into R_2 during the pulses, as a function of offset. Second, there is a faster fluctuation (with a "frequency" of about 0.5 ppm) that is caused by incompleteness of the spin echo due to finite pulse length, which causes severe effective field angle deviations that leaves part of the magnetization along the Z-axis in *between* the pulses hence admixing a large R_1 component and temporarily diminishing the apparent transverse component magnitudes. Since in macromolecules R_1 is always smaller than R_2 one thus sees mostly deviations that result in the reduction in the R_2 rate. Instances that the apparent R_2 exceeds the real R_2 (e.g., at ±4 ppm) are due to incomplete refocusing, hence causing an apparent faster decay. We now discuss the origins of the two deviations at different timescales in more detail.

3.1. Origin of the slow fluctuations: the effective-decay artifact

These slow artifacts are caused by the offset dependence of the instantaneous relative phase of the free precessing transverse magnetization with respect to the phase of the RF pulse. For example, on-resonance X-magnetization experiencing CPMG pulse train of pure X-phase will throughout the sequence stay aligned with the X-axis, and will yield $R_{2\text{-eff}}^{\text{Para}}$ (for parallel, $\pm X$-phase) which simply is

$$R_{2\text{-eff}}^{\text{Para}} = R_2. \qquad (5)$$

A spin vector off-resonance by an amount $\nu = (2\tau_{\text{cp}})^{-1}$, will move from the X-axis to the Y-axis before the first CPMG pulse, and remains to be refocused on the Y-axis before each pulse during the body of the CPMG

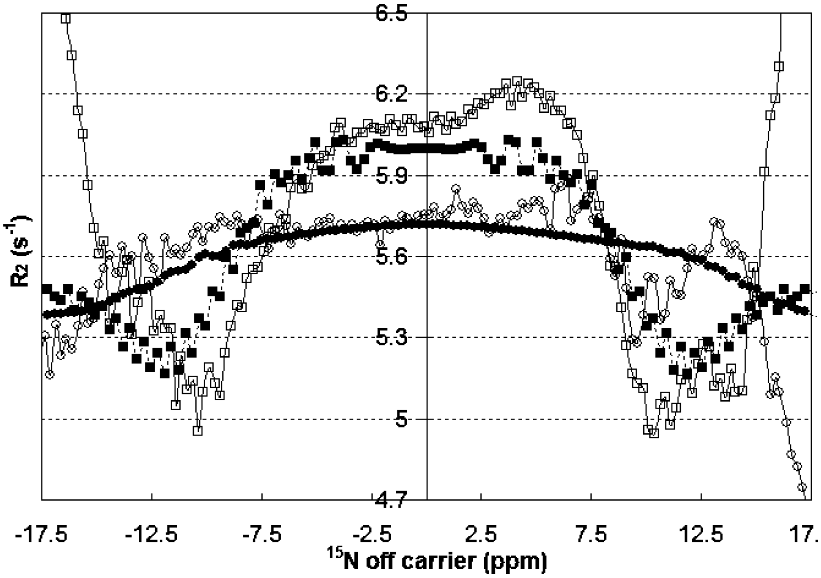

Fig. 5. Overlay of simulated (closed symbols) and experimental (one RF carrier position) (open symbols) R_2 offset dependency profiles for both [0, 0, 0, 0] (squares) and [0, 0, 1, 3] (circles) phase cycles. Simulated values are an average of five levels of simulated gradient profiles (180, 177.5, 175, 172.5, and 170) to simulate RF inhomogeneity. Experimental errors of the order of ±0.05 to ±0.1 ppm per standard deviation are not shown for viewing ease.

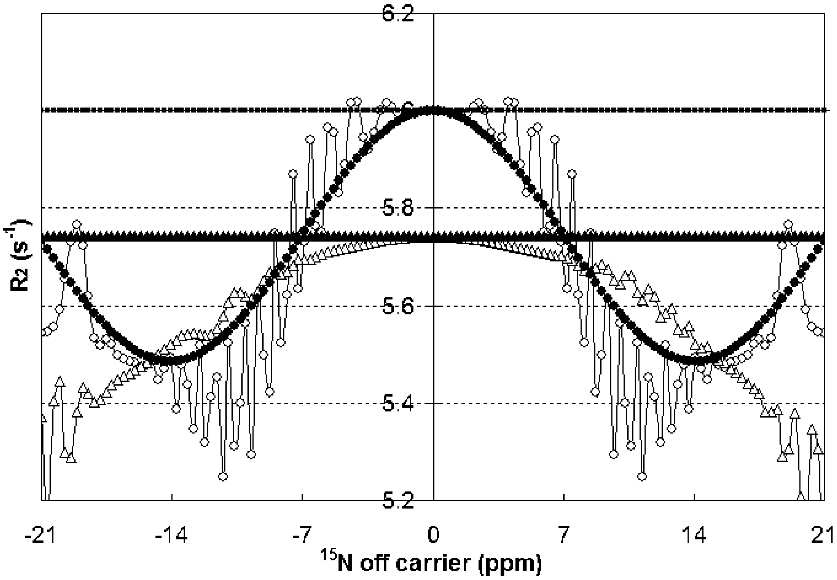

Fig. 6. Simulated (open symbols) R_2 offset dependence profiles of soft CPMG pulses (i.e., τ_π = 200 μs) of perfectly homogeneous samples for phase cycles [0, 0, 0, 0] (circles) and [0, 0, 1, 3] (triangles). The corresponding profiles (closed symbols) are described by Eq. (14) (circles) and Eq. (15) (triangles) for 0000 and 0013 cycles, respectively. The line at 6 s^{-1} represents the true R_2 rate.

sequence. This has the consequence that the X-phase CPMG π pulse will rotate the magnetization vector through Z, thus bestowing some R_1 relaxation character decay to the overall relaxation process. This is akin to an on-resonance X-magnetization experiencing a CPMG pulse of Y-phase causing the vector to rotate through Z, thus admixing R_1 and R_2 character decay. This is referred to as $R_{2\text{-eff}}^{\text{Ortho}}$ (for orthogonal, ±Y-phase):

$$R_{2\text{-eff}}^{\text{Ortho}}(\beta) = \frac{\int_0^\beta (R_2\cos^2\theta + R_1\sin^2\theta)\mathrm{d}\theta}{\int_0^\beta \mathrm{d}\theta}, \tag{6}$$

where θ is the instantaneous angle of the magnetization vector out of the transverse plane (Fig. 8) and Eq. (6) becomes

$$R_{2\text{-eff}}^{\text{Ortho}} = \frac{R_2 + R_1}{2}, \tag{7}$$

when $\beta = \pi$. Since R_1 is smaller than R_2 for any macromolecule, this results in an apparent reduction of R_2 during orthogonal RF pulse periods.

The problem of offset-dependent out-of-plane perturbation into the Z direction can be ameliorated by altering the phases of the CPMG pulses, thereby inducing uniform out-of-plane perturbation for all spin systems of distinctly different resonance offsets. In doing this, one should expect that the value of the R_2 observable would no longer be immediately accurate.

However, this is a very acceptable compromise, since it increases the *relative* reliability of the observations measured, spanning the spectral width range within a spectrum, from a single experiment. We have searched for the optimal phase train by systematically changing the CPMG phase cycle using computer simulations and selecting (by hand) the relatively minimal offset dependence. All combinations of 0, 1, 2, and 3 phases in repeat cycles of four CPMG pulses (a total of 256 phase cycles) were simulated and offset dependence R_2 profiles calculated, as described in Section 2. Of the 256 phase cycle combinations, only a few combinations emerged that provided reasonable offset dependence profiles. Consistent in all acceptable phase cycles is the basic phase cycle pairs, 00, 22, 13, and 31. It is vital that the two phases described by each basic pair is coupled, because detailed simulations reveal that these pairs are the only combinations that can provide a critical 'refocus' of the effective-field artifact behavior for off-resonance spins, especially for soft RF pulses. Of the 16 remaining combinations, the cycles of most stable offset dependence profiles are 0013 or 1300, 0031 or 3100, 2231 or 3122, and 2213 or 1322. Each pair of CPMG phase cycles correspond to schemes of equivalent offset dependence profiles; this is not surprising, since it is just the basic pair order swapped. Additionally, we not unexpectedly find that the negative initial magnetization offset profile of 0000 is equivalent to the positive magnetization 2222 profile, and negative magnetization 0013 is equivalent to positive magnetization 2231. Furthermore, due to the acquisition of ± phase cycling of the first ^{15}N pulse of the sequence per point in the t_1-^{15}N FID concomitant with the subtracting in the receiver (Fig. 3), the average of the R_2 rate from positive and negative magnetization values on the same phase cycle, or equivalent (i.e., average of +0000 and +2222, or +0013 and +2231), must be implemented. In the final analysis we arrive at the CPMG phase cycle [0, 0, 1, 3] (or [0, 0, 3, 1]).

Experimental data (Fig. 7) using the [0, 0, 1, 3] scheme demonstrates the superiority of the R_2 profile of the [0, 0, 1, 3] phase cycle scheme as it shows a significantly 'flatter' offset dependence. Relatively little offset dependence is seen for -10 to +7 ^{15}N ppm offset range while in the traditional phase cycle the same can be said only for a -4 to +3 ^{15}N ppm offset range. The new cycle thus yields a greater than factor of two improvement in offset independency range. As mentioned above, the new cycle allows for the consistent mixing of R_1 and R_2 over the different free-precession angles, so the R_2 measurements are not absolutely accurate and contain an R_1 component. However, since R_1 will commonly be known, we can derive the following equations to compute the true R_2 from the observations. Since in the [0, 0, 1, 3] cycle there are two parallel and two orthogonal pulses, we obtain, on-resonance

$$R_{2\text{-eff}}^{0013^{\text{On-Resonance}}} = \frac{2R_{2\text{-eff}}^{\text{Para}} + 2R_{2\text{-eff}}^{\text{Ortho}}}{4} = \frac{3R_2 + R_1}{4}, \tag{8}$$

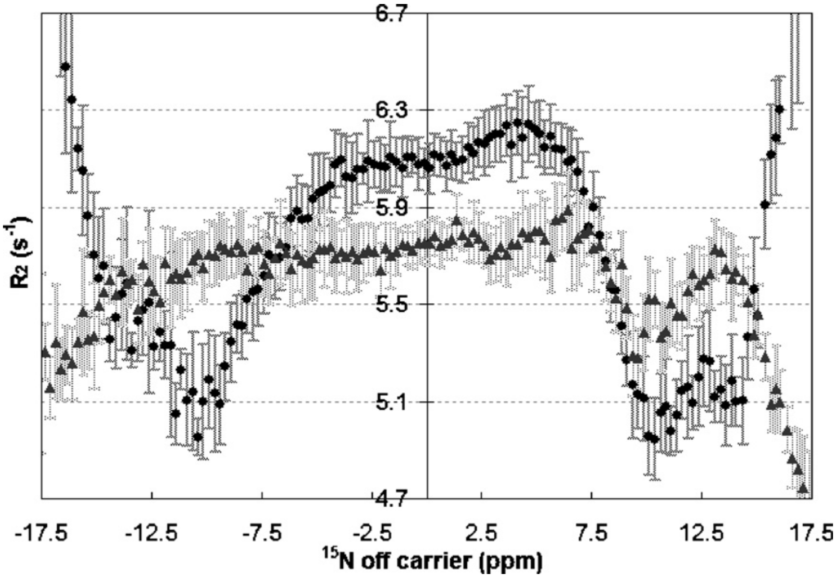

Fig. 7. Experimental standardized R_2 offset dependence profile plots of [0, 0, 0, 0] (circles) and [0, 0, 1, 3] (triangles) phase cycles schemes. Standardization (Procedure 1) was applied on these data. Displayed are 0.25 ppm width histogram averages with ±1 standard deviation of that average represented by the error bars.

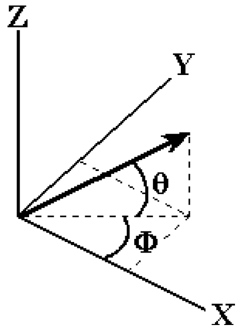

Fig. 8. Definitions of the angles θ and Φ used in the analytical derivations.

where $R_{2\text{-eff}}^{\text{Para}}$ and $R_{2\text{-eff}}^{\text{Ortho}}$ are defined in Eqs. (5) and (7). Similarly, the effective R_2 decay for the conventional pulse scheme [0, 0, 0, 0] is, on-resonance

$$R_{2\text{-eff}}^{0000^{\text{On-Resonance}}} = \frac{4R_{2\text{-eff}}^{\text{Para}}}{4} = R_2. \tag{9}$$

When we make the (temporary) assumption that the effective flip angle β is constant at π for all offsets and neglect free precession contributions ($\omega_{\text{FP}} = 0$) during the pulses, we can analytically solve for the offset dependency of the effective R_2 decay:

$$R_{2\text{-eff}}^{\text{Para}}(\Phi) = R_2\cos^2\Phi + \frac{R_2 + R_1}{2}\sin^2\Phi, \tag{10}$$

$$R_{2\text{-eff}}^{\text{Ortho}}(\Phi) = \frac{R_2 + R_1}{2}\cos^2\Phi + R_2\sin^2\Phi, \tag{11}$$

where the angle Φ represents the expected (free-precession) offset difference of the coherence (after $\tau_{\text{cp}}/2$) with respect to the initial magnetization direction (Fig. 8). It follows then that the effective R_2 during the four pulses for the two phase cycle schemes are described by

$$\begin{aligned} R_{2\text{-eff}}^{0000}(\Phi) &= \frac{4R_{2\text{-eff}}^{\text{Para}}(\Phi)}{4} = R_{2\text{-eff}}^{\text{Para}}(\Phi) \\ &= R_2\cos^2\Phi + \frac{R_2 + R_1}{2}\sin^2\Phi \end{aligned} \tag{12}$$

and

$$R_{2\text{-eff}}^{0013}(\Phi) = \frac{2R_{2\text{-eff}}^{\text{Para}}(\Phi) + 2R_{2\text{-eff}}^{\text{Ortho}}(\Phi)}{4} = \frac{3R_2 + R_1}{4}. \tag{13}$$

Taking the free precession during the inter-pulse spacing $2\tau_{\text{FP}}$ ($\tau_{\text{cp}} = \tau_{\text{FP}} + \tau_\pi + \tau_{\text{FP}}$) into account, one finally arrives at (neglecting the difference between in-phase and anti-phase R_2 relaxation during free precession)

$$\begin{aligned} R_{2\text{-eff}}^{\text{CPMG}^{0000}}(\Phi) &= \frac{\tau_\pi R_{2\text{-eff}}^{0000}(\Phi) + 2\tau_{\text{FP}}R_2}{\tau_\pi + 2\tau_{\text{FP}}} \\ &= \frac{\left(\tau_\pi\cos^2\Phi + \frac{1}{2}\tau_\pi\sin^2\Phi + 2\tau_{\text{FP}}\right)R_2 + \left(\frac{1}{2}\tau_\pi\sin^2\Phi\right)R_1}{\tau_{\text{cp}}} \end{aligned} \tag{14}$$

and

$$\begin{aligned} R_{2\text{-eff}}^{\text{CPMG}^{0013}}(\Phi) &= \frac{\tau_\pi R_{2\text{-eff}}^{0013}(\Phi) + 2\tau_{\text{FP}}R_2}{\tau_\pi + 2\tau_{\text{FP}}} \\ &= R_2 + \frac{(R_1 - R_2)\tau_\pi}{4\tau_{\text{cp}}}, \end{aligned} \tag{15}$$

where τ_π is the duration of the π pulse. Comparison of Eqs. (14) and (15) shows that the conventional [0 0 0 0] phase cycle scheme is dependent on Φ (i.e., free precession offset effects). As anticipated, the effective R_2 for the [0 0 1 3] CPMG pulse scheme is independent of Φ because of the equal balance of orthogonal and parallel evolution from the mixed phase cycling. Fig. 6 shows that Eqs. (14) and (15) do describe the offset dependence of the Bloch-simulated sequences quite well. Deviations between the simulated and analytical curves are due to the fact that the simulated Bloch curves, in contrast to analytical equations, do take the offset dependence of the effective flip angle and ω_{FP} terms of the pulses into account.

Only at on-resonance will the analytical corrections derived above absolutely correspond to realistic observations, since there is no effective-field difference. However, our calculation allows a simple correction that can be applied to the observable from the entire range of -10 to $+7$ ^{15}N ppm. The first is already pointed out by the fact that our new scheme correction is independent of Φ, so theoretically the scheme sufficiently eliminates any offset dependence variability from effective-decay artifact, but simplifies the artifact effect to a constant amount for all offsets.

A further advantage is that the fast modulations mentioned above and discussed more below, are dramatically suppressed in the 0013 scheme because the mixing of parallel and orthogonal evolutions which have, in effect, dephased it. The fast modulation components cannot be discerned in the experimental data (Fig. 5 or 7). This is likely due to the fact that the experimental signal to noise ratio is insufficient to disclose these fluctuations. Second, the simulated dependence profiles are computed for ideal RF amplitude and phase homogeneity throughout the sample, which is certainly not the case in the real experiment. In the simulated curves of Fig. 5 we demonstrate that RF inhomogeneity (modeled by averaging curves obtained with five different flip angles) does indeed destructively interferes with the fluctuations. Thus, in simulation and practice, the fast fluctuations seen in Fig. 6 are of no real concern.

3.2. Origin of the fast fluctuations: the effective-field artifact

Far off-resonance, the RF phase and flip angle, start to deviate from ideality. In combination with the different instantaneous angles between the free precessing coherence and the RF phase as a function of offset, and the varying number of RF pulses that constitute a relaxation series, the spin physics becomes very complicated indeed. First of all, it is disturbing to note that the relaxation decay curve itself can become modulated for spin systems of specific offset displacement; for instance the modulation seen in Fig. 4 makes the extraction of a single exponential relaxation rate questionable. While the application of the new CPMG phase scheme does improve the situation somewhat, we note that correction of the decay curves at this offset is useless, as much larger errors are introduced by convoluted and irregular spin echo behavior.

The main artifact far off-resonance stems from the fact that the magnetization vectors are not subject to proper 180° rotations. The outcome of is the lack of return of the magnetization vector into the transverse plane, and with multiple back-to-back spin echoes the magnetization vector effectively experiences an out-of-plane modulation throughout the magnetization decay (this is one of the causes of the oscillations in Fig. 4). Furthermore, the frequency and amplitude of the decay profile modulation is likewise offset dependent, accounting for the fast modulations seen in the simulated conventional phase cycle R_2 dependence profile (Fig. 6). These modulations are not random, and appear to be suppressed somewhat in the mixed (0 0 1 3) pulse schemes, leading to less modulations of R_2 profile as a function of resonance offset (Fig. 6).

The effective-field artifacts can only have impact during the pulse period, but because of the severity of leaving the position of the magnetization vector out of the transverse plane between pulses, it inadvertently causes varying intermixing of R_1 and R_2 decay on the spin system at all times. Ultimately, it is the resulting diminished magnitude of the transverse components from having the vector left out of the transverse plane that causes the oscillations in the decay profile and consequently causing the fast oscillations seen in the simulated offset dependence profile (Fig. 9). The problem originates from the ω_{FP} terms contaminating the proper spin echo behavior. Indeed, if R_2 and R_1 were set equal, the effective-decay artifact R_2 CPMG contributions become $R_{2\text{-eff}}^{\mathrm{CPMG}^{0000}}(\Phi) = R_{2\text{-eff}}^{\mathrm{CPMG}^{0013}}(\Phi) = R_2$, a constant independent of Φ; all that will remain is the fast oscillating effective-field artifact influence on the offset dependence profiles (Fig. 9). If all ω_{FP} terms were to be set to zero only during the pulse period, in other words, if no precession would take place during the pulse, the resulting simulated R_2 dependence profile as well as the decay profiles no longer experience the fast oscillations (Fig. 9). All that remain is the effective-decay artifact offset dependence.

While the [0 0 1 3] phase cycle suppresses both the effective decay and effective field artifacts, the behavior far off-resonance (>|7.5 ppm|) is still not ideal, neither in reality (Fig. 7) nor in Bloch simulation (Fig. 6). Despite the fact that $R_{2\text{-eff}}^{\mathrm{CPMG}^{0013}}(\Phi)$ is independent of Φ, experimentally there is a degrading dependence of the R_2 value further offset simply because of the greater strength of the effective-field artifact influence as Φ increases, which is simply not accounted for in the analytical correction of Eq. (15). The bottom line is, that R_2

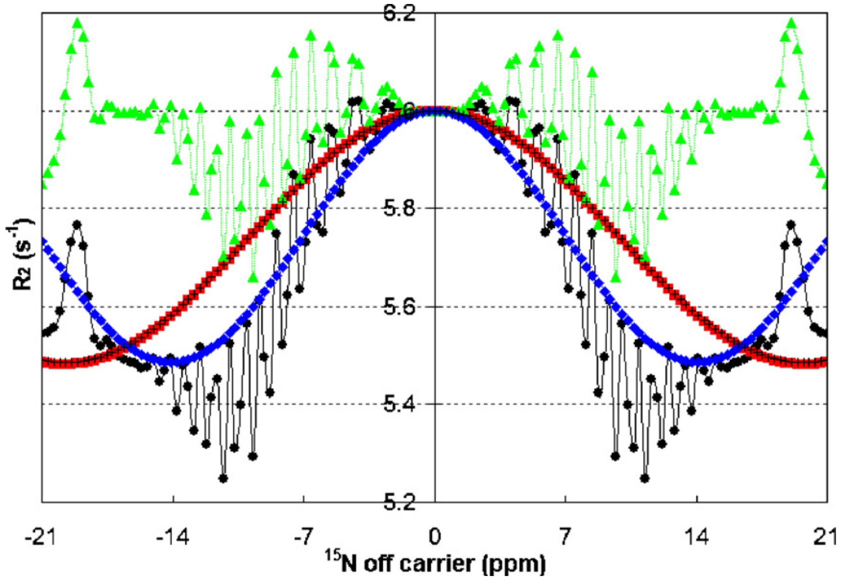

Fig. 9. Shown are simulated 0000 phase cycle R_2 offset dependence profiles for: all artifacts accountable (black circles); effective-decay artifact influence only or $\omega_{\mathrm{FP}} = 0$ during the pulse period (red squares); and effective-field artifact influence only or $R_2 = R_1 = 6\ \mathrm{s}^{-1}$ (green triangles). Also displayed are plots of Eq. (14): as a function of Φ = expected angle offset difference after $\tau_{\mathrm{cp}}/2$ (blue diamonds); and as a function of $\Phi\tau_{\mathrm{FP}}$ = expected angle offset difference after τ_{FP} (black crosses). (For interpretation of the references to colour in this figure legend, the reader is referred to the web version of this paper.)

CPMG rates can just not be measured properly at these large offsets neither with the classical scheme nor with the new [0 0 1 3] scheme.

It should not be surprising that the offset profiles for [0 0 1 3] is asymmetric around the carrier position; despite the fact that phase cycling of the first ^{15}N 90° pulse carries out some symmetrization, the '13' component is not sufficiently symmetrized because the average of the positive and negative magnetization as produced by this cycling only averages 0013 and 2231. A secondary averaging is required, namely 0031 and 2213, to thoroughly average out all asymmetry. Thus, a more complete phase cycle of 00130031 in the CPMG train, coupled with magnetization inversion as afforded by the first ^{15}N pulse, is necessary to produce a symmetric offset dependency profile (results not shown).

From the conclusions above we can predict the performance at different limits of the CPMG experiment. First, it is important to understand the amplitude and variation of the offset dependence relative to the pulse strength. In Fig. 10, we show that the total amplitude of the modulations (from both artifact types; slow and fast) on the profile is directly proportional to the length of the pulse (keeping τ_{cp} constant). To state the obvious, the R_2-CPMG experimental technique becomes perfect for all offsets in the limit of infinite RF pulse power. However, the [0 0 1 3] scheme still significantly suppresses the fast modulations seen in [0 0 0 0] when using an (unattainable) 25 μs 180° ^{15}N pulse, and hence, can extend the relative reliability offset range even for this (impossible) experiment. As extensively demonstrated above, when using soft pulses, the difference between the [0 0 0 0] and [0 0 1 3] schemes are dramatic indeed.

Second, we have so far only investigated the artifacts at a constant relatively short τ_{cp} (700 μs) period, which is towards the limit of spin-lock $T_{1\rho}$ experiments. In CPMG relaxation dispersion experiments, the τ_{cp} period is varied to obtain the rate of the dynamic (kinetic) process. For the relaxation dispersion experiments, it is obviously important that, at the very least, the offset dependence profile be consistent for the range of τ_{cp} values that is used. Regretfully, this is not found to be the case. However, Fig. 11 demonstrates the superiority of our proposed [0 0 1 3] phase scheme compared to the conventional scheme, not only by the fact that the fast modulations are almost completely suppressed, but that, most importantly, the dependence profiles for different τ_{cp} settings strongly coincide, after applying the simple 'shift' correction defined by Eq. (15). Conversely, the conventional scheme not only modulates, but the amplitude and frequency of its modulation changes for varying τ_{cp}, which extremely complicates the dependence profile at offset frequencies larger then ±3–4 ppm from the carrier. Finally, it should be mentioned that the [0 0 1 3] phase technique can easily be implemented the latest in-phase/anti-phase relaxation compensation schemes [25], CO CPMG [26,27] schemes, and multiple quantum CPMG schemes [27–29].

4. Conclusion

In conclusion, very significant artifacts have been revealed and analyzed for the evolution of spin magnetization vectors in the R_2-CPMG sequence by using numerical integration of the Bloch equations. The arti-

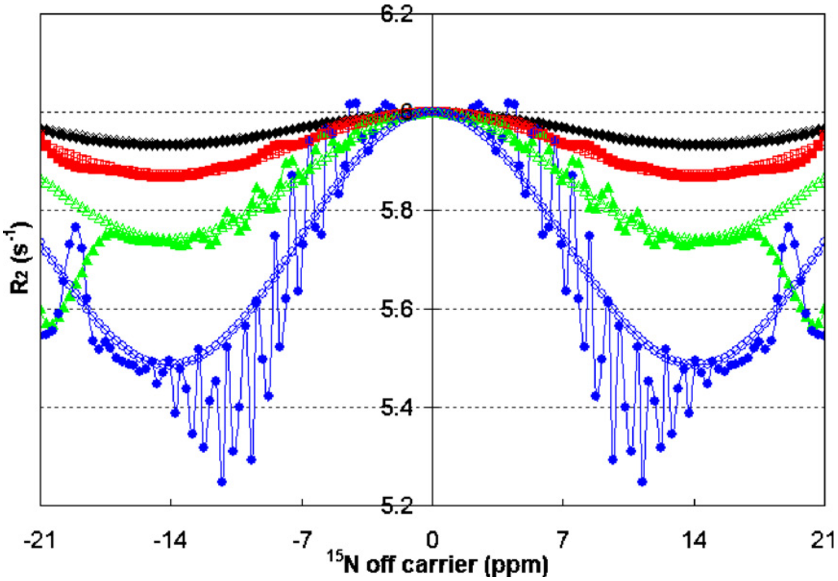

Fig. 10. Simulated [0 0 0 0] phase cycle R_2 offset dependence profiles of various RF field strengths at a constant τ_{cp} time of 700 μs. The uncorrected simulated profiles (closed symbols) and the corresponding plots of Eq. (14) as a function of Φ (open symbols) are shown for the following 180° RF pulse strengths of length: 25 μs (black diamonds), 50 μs (red squares), 100 μs (green triangles), and 200 μs (blue circles). (For interpretation of the references to colour in this figure legend, the reader is referred to the web version of this paper.)

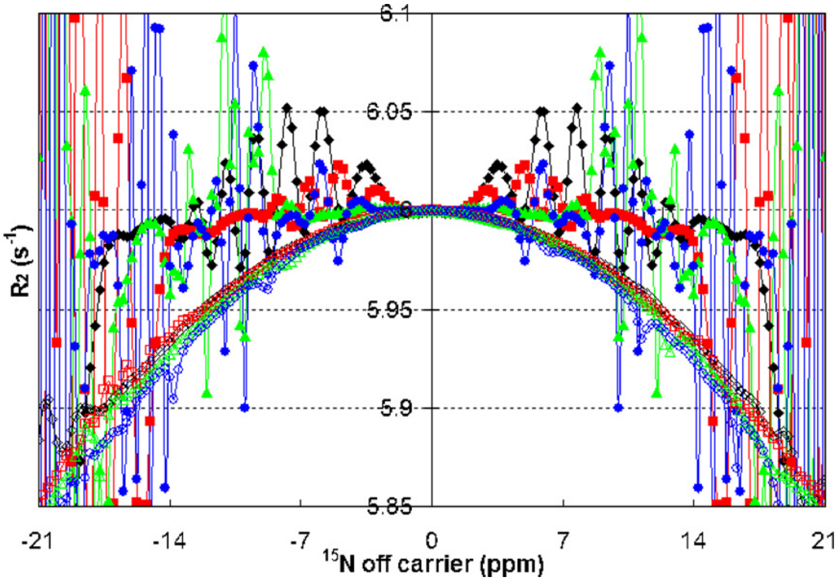

Fig. 11. Simulated R_2 offset dependence profiles of various τ_{cp} pulse repeat times at constant pulse strength of 100 μs 180°. The offset artifacts for the [0 0 0 0] phase cycle (closed symbols) and the [0 0 1 3] phase cycle (open symbols) are shown for the following τ_{cp}: 700 μs (black diamonds), 1 ms (red squares), 2 ms (green triangles), and 4 ms (blue circles). (For interpretation of the references to colour in this figure legend, the reader is referred to the web version of this paper.)

facts are easily of a magnitude that they can lead to the wrong conclusions with respect protein dynamics on both nanosecond timescale as well as on the millisecond time scale. All artifacts have in common, trivially that they can be substantially suppressed by using very strong RF pulses in the CPMG cycle; however this solution may not be a practical one, depending on instrument, sample and probe type.

The main message of our contribution is that all artifacts also have in common that they can be substantially suppressed by a simple change in the phase cycle of the CPMG train; instead of applying a $[0\,0\,0\,0]^N$ cycle, the cycle $[0\,0\,1\,3]^N$ or more completely the cycle $[0\,0\,1\,3\,0\,0\,3\,1]^{N/2}$ effectively more than doubles the spectral width for which the R_2 rates can be relatively reliably determined using a single RF carrier setting. Our proposed scheme is also robust towards changes in τ_{cp}, allowing for more reliable relaxation dispersion experiments. Moreover, the implementation of the new scheme allows the extension of the relaxation dispersion technique to measure slow dynamic processes of tens of milliseconds. As the only drawback, the new cycle introduces a R_1 component in the otherwise "flat" experimental R_2 rates (reducing the apparent R_2 by about 5%). Herein, we give equations that can analytically correct for this intermixing if the R_1 is known.

Acknowledgments

This work was supported by NIH GM 52421, and by the DOE "From Genome to Life" project grant, subproject "Fast determination of protein complexes by NMR." We thank Dr. Alex Kurochkin for the maintenance of the NMR spectrometers, Dr. Tianzhi Wang for valuable discussions, and the W.F. Keck foundation for funds towards the purchase of the NMR spectrometers used.

References

[1] M.W.F. Fischer, A. Majumdar, E.R.P. Zuiderweg, Protein NMR relaxation: theory, applications and outlook, Prog. Nucl. Mag. Reson. Spectroscopy 33 (1998) 207–272.
[2] A.G. Palmer, Probing molecular motion by NMR, Curr. Opin. Struct. Biol. 7 (1997) 732–737.
[3] E.R.P. Zuiderweg, Mapping protein–protein interactions in solution by NMR Spectroscopy, Biochemistry 41 (2002) 1–7.
[4] A.M. Mandel, M. Akke, A.G. Palmer, Backbone dynamics of *Escherichia-coli* ribonuclease hi-correlations with structure and function in an active enzyme, J. Mol. Biol. 246 (1995) 144–163.
[5] S.Y. Stevens, S. Sanker, C. Kent, E.R.P. Zuiderweg, Delineation of the allosteric mechanism of a cytidylyltransferase exhibiting negative cooperativity, Nat. Struct. Biol. 8 (2001) 947–952.
[6] J. Cavanagh, M. Akke, May the driving force be with you—whatever it is, Nat. Struct. Biol. 7 (2000) 11–13.
[7] R. Ishima, D.A. Torchia, Protein dynamics from NMR, Nat. Struct. Biol. 7 (2000) 740–743.
[8] L.E. Kay, Protein dynamics from NMR, Nat. Struct. Biol. 5 (1998) 513–517.
[9] Y. Pang, M. Buck, E.R.P. Zuiderweg, Backbone dynamics of the ribonuclease binase active site area using multinuclear (N-15 and (CO)-C-13) NMR relaxation and computational molecular dynamics, Biochemistry 41 (2002) 2655–2666.
[10] A.G. Palmer 3rd., C.D. Kroenke, J.P. Loria, Nuclear magnetic resonance methods for quantifying microsecond-to-millisecond motions in biological macromolecules, Methods Enzymol. 339 (2001) 204–238.

[11] D. Kern, E.R. Zuiderweg, The role of dynamics in allosteric regulation, Curr. Opin. Struct. Biol. 13 (2003) 748–757.

[12] C.H. Papavoine, M.L. Remerowski, L.M. Horstink, R.N. Konings, C.W. Hilbers, F.J. van de Ven, Backbone dynamics of the major coat protein of bacteriophage M13 in detergent micelles by 15N nuclear magnetic resonance relaxation measurements using the model-free approach and reduced spectral density mapping, Biochemistry 36 (1997) 4015–4026.

[13] D. Jin, M. Andrec, G.T. Montelione, R.M. Levy, Propagation of experimental uncertainties using the Lipari-Szabo model-free analysis of protein dynamics, J. Biomol. NMR 12 (1998) 471–492.

[14] D.M. Korzhnev, V.Y. Orekhov, A.S. Arseniev, Model-free approach beyond the borders of its applicability, J. Magn. Reson. 127 (1997) 184–191.

[15] Y.E. Shapiro, E. Kahana, V. Tugarinov, Z. Liang, J.H. Freed, E. Meirovitch, Domain flexibility in ligand-free and inhibitor-bound *Escherichia coli* adenylate kinase based on a mode-coupling analysis of 15N spin relaxation, Biochemistry 41 (2002) 6271–6281.

[16] V. Tugarinov, Z. Liang, Y.E. Shapiro, J.H. Freed, E. Meirovitch, A structural mode-coupling approach to 15N NMR relaxation in proteins, J. Am. Chem. Soc. 123 (2001) 3055–3063.

[17] R. Ishima, D.A. Torchia, Extending the range of amide proton relaxation dispersion experiments in proteins using a constant-time relaxation-compensated CPMG approach, J. Biomol. NMR 25 (2003) 243–248.

[18] F.A. Mulder, N.R. Skrynnikov, B. Hon, F.W. Dahlquist, L.E. Kay, Measurement of slow (micros-ms) time scale dynamics in protein side chains by (15)N relaxation dispersion NMR spectroscopy: application to Asn and Gln residues in a cavity mutant of T4 lysozyme, J. Am. Chem. Soc. 123 (2001) 967–975.

[19] M.J. Grey, C. Wang, A.G. Palmer 3rd, Disulfide bond isomerization in basic pancreatic trypsin inhibitor: multisite chemical exchange quantified by CPMG relaxation dispersion and chemical shift modeling, J. Am. Chem. Soc. 125 (2003) 14324–14335.

[20] F. Massi, E. Johnson, C. Wang, M. Rance, A.G. Palmer 3rd., NMR R1 rho rotating-frame relaxation with weak radio frequency fields, J. Am. Chem. Soc. 126 (2004) 2247–2256.

[21] D.M. Korzhnev, E.V. Tischenko, A.S. Arseniev, Off-resonance effects in N15 T2 CPMG measurements, J. Biomol. NMR 17 (2000) 231–237.

[22] A. Ross, M. Czisch, G.C. King, Systematic errors associated with the CPMG pulse sequence and their effect on motional analysis of biomolecules, J. Magn. Reson. 124 (1997) 355–365.

[23] M. Czisch, G.C. King, A. Ross, Removal of systematic errors associated with off-resonance oscillations in T2 measurements, J. Magn. Reson. 126 (1997) 154–157.

[24] F. Bloch, Nuclear induction, Phys. Rev. 70 (1946) 460–474.

[25] J.P. Loria, M. Rance, A.G. Palmer, A relaxation-compensated Carr-Purcell-Meiboom-Gill sequence for characterizing chemical exchange by NMR spectroscopy, J. Am. Chem. Soc. 121 (1999) 2331–2332.

[26] R. Ishima, J. Baber, J.M. Louis, D.A. Torchia, Carbonyl carbon transverse relaxation dispersion measurements and ms-micros timescale motion in a protein hydrogen bond network, J. Biomol. NMR 29 (2004) 187–198.

[27] H. Koskela, I. Kilpelainen, S. Heikkinen, LR-CAHSQC: an application of a Carr-Purcell-Meiboom-Gill-type sequence to heteronuclear multiple bond correlation spectroscopy, J. Magn. Reson. 164 (2003) 228–232.

[28] K.H. Lim, T. Nguyen, T. Mazur, D.E. Wemmer, A. Pines, Sensitivity enhancement in multiple-quantum NMR experiments with CPMG detection, J. Magn. Reson. 157 (2002) 160–162.

[29] D.M. Korzhnev, K. Kloiber, V. Kanelis, V. Tugarinov, L.E. Kay, Probing slow dynamics in high molecular weight proteins by methyl-TROSY NMR spectroscopy: application to a 723-residue enzyme, J. Am. Chem. Soc. 126 (2004) 3964–3973.